

See discussions, stats, and author profiles for this publication at: <https://www.researchgate.net/publication/322934086>

# InSAR and GPS derived coseismic deformation and fault model of the 2017 Ms7.0 Jiuzhaigou earthquake in the Northeast Bayanhar block

Article in *Tectonophysics* · February 2018

DOI: 10.1016/j.tecto.2018.01.026

CITATIONS

24

READS

655

6 authors, including:



**Dezheng Zhao**

Institute of Geology, China Earthquake Administration

17 PUBLICATIONS 64 CITATIONS

[SEE PROFILE](#)



**Xinjian Shan**

China Earthquake Administration

235 PUBLICATIONS 1,416 CITATIONS

[SEE PROFILE](#)



**Wenyu Gong**

University of Alaska Fairbanks

44 PUBLICATIONS 295 CITATIONS

[SEE PROFILE](#)



**Yingfeng Zhang**

155 PUBLICATIONS 3,304 CITATIONS

[SEE PROFILE](#)

Some of the authors of this publication are also working on these related projects:



Initiative Sensing and Dynamic Optimization Method for the Execution of Internet of Manufacturing Things [View project](#)



Call for papers for a special volume of the Journal of Cleaner Production: Sustainable product lifecycle management based on smart enabling technologies [View project](#)



# InSAR and GPS derived coseismic deformation and fault model of the 2017 Ms7.0 Jiuzhaigou earthquake in the Northeast Bayanhar block

Dezheng Zhao, Chunyan Qu\*, Xinjian Shan, Wenyu Gong, Yingfeng Zhang, Guohong Zhang

State Key Laboratory of Earthquake Dynamics, Institute of Geology, China Earthquake Administration, Beijing 100029, China

## ARTICLE INFO

### Keywords:

Jiuzhaigou earthquake  
InSAR coseismic deformation  
Fault slip model  
Sentinel-1A  
Coulomb stress change

## ABSTRACT

On 8 August 2017, a Ms7.0 earthquake stroke the city of Jiuzhaigou, Sichuan, China. The Jiuzhaigou earthquake occurred on a buried fault in the vicinity of three well-known active faults and this event offers a unique opportunity to study tectonic structures in the epicentral region and stress transferring. Here we present coseismic displacement field maps for this earthquake using descending and ascending Sentinel-1A Interferometric Synthetic Aperture Radar (InSAR) data. Deformation covered an area of approximately  $50 \times 50$  km, with a maximum line-of-sight (LOS) displacement of  $\sim 22$  cm in ascending and  $\sim 14$  cm in descending observations on the west side of the source fault. Based on InSAR and Global Positioning System (GPS) measurements, both separately and jointly, we constructed a one-segment model to invert the coseismic slip distribution and dip angle of this event. Our final fault slip model suggests that slip was concentrated at an upper depth of 15 km; there was a maximum slip of  $\sim 1.3$  m and the rupture was dominated by a left-lateral strike-slip motion. The inverted geodetic moment was approximately  $6.75 \times 10^{18}$  Nm, corresponding to a moment magnitude of Mw6.5, consistent with seismological results. The calculated static Coulomb stress changes indicate that most aftershocks occurred in stress increasing zones caused by the mainshock rupture; the Jiuzhaigou earthquake has brought the western part of the Tazang fault 0.1–0.4 MPa closer to failure, indicating an increasing seismic hazard in this region. The Coulomb stress changes caused by the 2008 Mw7.8 Wenchuan earthquake suggest that stress loading from this event acted as a trigger for the Jiuzhaigou earthquake.

## 1. Introduction

A moderate earthquake with a magnitude of Ms7.0 struck Jiuzhaigou County, Sichuan, China on 8 August 2017. Its epicentre was located  $33.2^\circ\text{N}$  and  $103.88^\circ\text{E}$ , and it had a focal depth of 20 km (<http://www.csi.ac.cn/>). The event, which resulted in 25 casualties and > 250 injuries, represents one in a series of strong intraplate earthquakes that have occurred on the eastern boundary of the Bayanhar block since the 2013 Mw6.6 Lushan earthquake and the 2008 Mw7.8 Wenchuan earthquake (Fig. 1a). According to the aftershock sequence recorded by the Sichuan Seismic Network, 31  $M > 3$  aftershocks occurred within 10 days of this event, the largest a M4.8 event (<http://www.scdzj.gov.cn/dzpd/dzzj/ljysdzzt2775/>). Preliminary teleseismic waveform analysis suggested that the rupture process for this event occurred on a left-lateral strike-slip buried fault; the maximum slip was  $\sim 0.6$  m, occurring at a depth of  $\sim 15$  km (<http://www.cea-igp.ac.cn/>). Focal mechanism solutions from different organisations have also indicated coseismic rupture caused by left-lateral strike-slip movement (Table. 1). However, the seismogenic fault responsible for this event has not been identified

or studied.

The Ms7.0 Jiuzhaigou earthquake occurred on the northern section of the eastern border of the Bayanhar block, within the Tibetan Plateau (Fig. 1a). Eastward crustal extrusion and the intense deformation of the active Bayanhar block have caused several strong earthquakes ( $M > 7.0$ ) along the block boundary faults, including the 2008 Mw7.8 Wenchuan, the 2001 Mw7.8 Kokoxili, and the 2013 Mw6.6 Lushan earthquakes (Fig. 1a; Deng et al., 2010; Lasserre et al., 2005; Xie et al., 2013; Xu et al., 2009). This area contains many branch faults and complex structures. The Huya fault, the Tazang fault, and the Minjiang fault are all major active faults in this region (Fig. 1b). Historically, ruptures have occurred on the Huya fault and on the Minjiang fault further to the south, including the 1933 Diexi Ms7.5 earthquake, the 1976 Songpan earthquake swarm ( $M = 7.2, 6.7, 7.2$ ), and the 1973 Songpan Ms6.5 earthquake (Fig. 1b; Li et al., 1979; Tang and Lu, 1981; Tang et al., 1983a, b). The Tazang fault is a Holocene active fault; its western segment is characterised by strike-slip movement, while the eastern segment demonstrates a thrust mechanism (Ren et al., 2013). It has lower slip rates of  $\sim 0.3$ – $1.5$  mm/yr along the eastern segment (i.e.,

\* Corresponding author.

E-mail address: [dqchy@ies.ac.cn](mailto:dqchy@ies.ac.cn) (C. Qu).

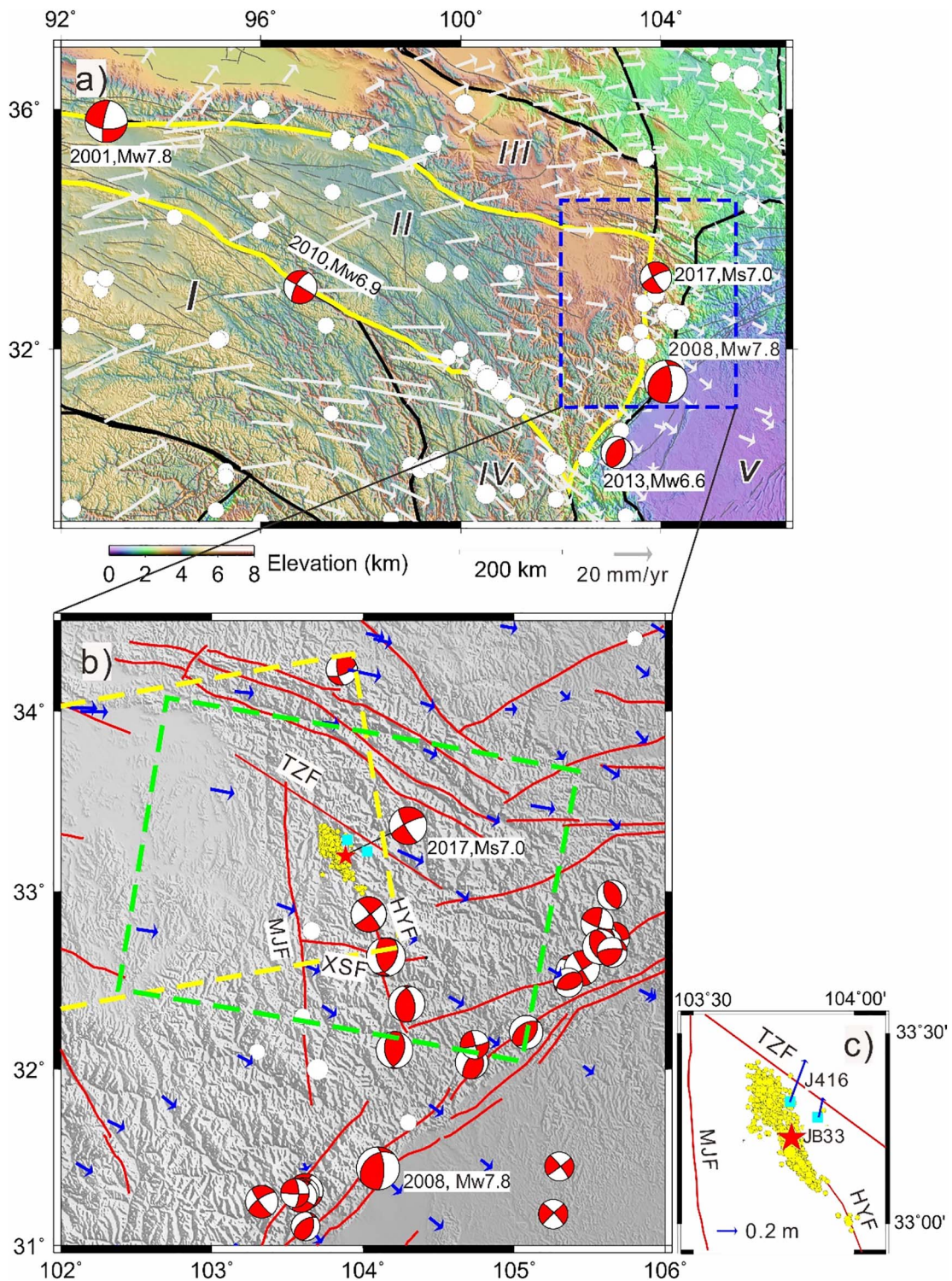


**Fig. 1.** Study area maps. (a) Tectonic map of the eastern Tibetan Plateau. Beach balls denote Global Centroid Moment Tensors (GCMT, from <http://www.globalcmt.org/CMTsearch.html>) of four large events ( $> M6.5$ ) and for the 2017 Jiuzhaigou earthquake. Black and yellow bold lines indicate the boundaries of subblocks, including the Qiangtang (I), Bayanhar (II), Kunlun-Qaidam (III), Chuandian (IV), and Huanan (V) blocks. Grey lines represent active faults. The blue dashed-line rectangle denotes the study area. (b) Enlarged topographic map of the Tazang fault (TZF), the Minjiang fault (MJF), the Huya fault (HYF), and the Xueshan fault (XSF). Yellow and green dashed-line boxes show the coverage of S1A SAR data. Cyan squares denote the locations of *Global Positioning System* (GPS) sites. Yellow circles denote relocated aftershocks following the Jiuzhaigou mainshock (Fang et al., 2017). Beach balls show the moment tensor of the Jiuzhaigou and historical earthquakes. The white dots in (a) and (b) show the locations of historical events. Horizontal component GPS velocity vectors relative to stable Eurasia in (a) and (b) are from Gan et al. (2007). (c) Horizontal coseismic displacements observed by GPS stations J416 and JB33. Epicenters are denoted by red stars. (For interpretation of the references to colour in this figure legend, the reader is referred to the web version of this article.)

**Table 1**  
Focal mechanism solutions for the Jiuzhaigou event.

Source <sup>a</sup>	Mw	Depth (km)	Fault plane 1			Fault plane 2		
			Strike (°)	Dip (°)	Rake (°)	Strike (°)	Dip (°)	Rake (°)
GCMT	6.5	14.9	242	77	−168	150	78	−13
USGS	6.5	13.5	246	57	−173	153	84	−33
IPGP		8	244	81	−165	151	75	−9
CEAIGP	6.5	19.2	65	82	−137	328	48	−11

<sup>a</sup> GCMT = Global Centroid Moment Tensors; USGS = United States Geological Survey; IPGP = Institut de Physique du Globe de Paris; CEAIGP = Institute of Geophysics, China Earthquake Administration.

the thrust component) and  $\sim 2.9$  mm/yr on the western segment (Harkins et al., 2010; Ren et al., 2013). Some of the east–west strike-slip motion on the Tazang fault has transferred into east–west compression of the Minjiang and Huya faults (Kirby et al., 2007; Kirby and Harkins, 2013). The Minjiang fault is a thrust fault with a slight left-lateral strike-slip component (Zhou et al., 2000). The northern segment of the Huya fault is dominated by left-lateral strike-slip movement, while the southern segment is characterised by thrust movement (Ren et al., 2013; Zhu and Wen, 2009). The Jiuzhaigou earthquake, which was the largest event in this region for 40 years, occurred in the area delimited by these three active faults (Fig. 1b). There are no surface traces of active faults in the epicentral area of the current tectonic map because of difficulties in geological investigation (Fig. 1b). Whether this event was caused by these three active faults or by another buried fault remains debated.

The epicentre of the Ms7.0 Jiuzhaigou earthquake was located in a mountainous region with an average elevation of  $> 4$  km. The dense coverage of vegetation, steep terrain, and sparse distribution of Global Positioning System (GPS) stations make it difficult to acquire and investigate coseismic surface deformation in this region (Fig. 1b). Field investigations were carried out immediately after the earthquake, but no obvious surface ruptures were found. In this case, InSAR is a key tool for obtaining the coseismic displacement field and for improving our understanding of the nature of faulting. Combined with ascending and descending InSAR observations, near-field high-density geodetic measurements can give robust constraints on fault geometry and slip distribution inversion at depth (Jiang et al., 2013; Wen et al., 2013). In addition, the estimation of the Coulomb stress changes on surrounding faults based on slip distribution is important for seismic hazard assessment.

The faulting and characteristics of the seismogenic fault of the 2017 Ms7.0 Jiuzhaigou earthquake remain poorly understood. Focal mechanism solutions suggest that the earthquake ruptured along a NNW trending fault with a primarily left-lateral strike-slip mechanism and varied dip angles (Table 1). However, the relocated aftershocks indicate a high-dip-angle fault plane (Fig. 2). In this study, we acquired coseismic displacement fields caused by the Ms. 7.0 Jiuzhaigou earthquake using both ascending and descending Sentinel-1A (S1A) InSAR observations. This approach has been successfully utilised in previous earthquake studies, including those focused on the 2015 Nepal Mw7.5 earthquake and the 2015 Chile Mw8.3 earthquake (e.g., Grandin et al., 2015; Solaro et al., 2016). SAR data combined with GPS measurements were further utilised to model and invert slip distribution at depth, and then to calculate the coseismic Coulomb stress changes for this event.

## 2. Data and coseismic deformation

The InSAR dataset in this study consists of four SAR acquisitions; two from ascending orbits on 30 July 2017 and 11 August 2017, and two from descending orbits on 6 August 2017 and 18 August 2017. The detailed parameters of the S1A data are shown in Table 2. S1A carries a C-band microwave sensor running in Terrain Observation with Progressive Scans (TOPS) mode. It has a large spatial coverage (i.e.,

250 km) with a repeat time of 12 days (De Zan and Monti Guarnieri, 2006). By utilising the available S1A Single Look Complex (SLC) images, we generated two D-InSAR interferograms using the GAMMA package with multilook factors of two and ten in the azimuth and range directions, respectively (Werner et al., 2000). To compensate for the residual azimuth phase ramp due to possible mis-registration in the azimuth direction, the Enhanced Spectral Diversity method was applied in overlapping areas across adjacent bursts (Prats-Iraola et al., 2012). We removed the effects of topography from interferograms using a 3-arc-second Shuttle Radar Topography Mission (SRTM) DEM. The interferograms were then filtered using a power spectrum method (Goldstein and Werner, 1998), followed by unwrapping with the minimum cost flow algorithm (MCF; Werner et al., 2000). The unwrapped interferograms were then geocoded to geodetic coordinates.

The differential InSAR (DInSAR) interferograms and deformation maps (Fig. 3) show some incoherent regions in the near-field of the seismogenic fault, but clear interferometric fringes caused by the 2017 Jiuzhaigou earthquake in both ascending and descending interferograms (Fig. 3a and c). Low coherence is mainly due to a combination of dense vegetation coverage and steep terrain in the epicentral area. The clear fringes are asymmetric on both sides of the source fault with a NW strike, implying a seismogenic fault in a NW direction across the coseismic displacement field and different movement features across this seismogenic fault. The whole displacement field covers an area of approximately  $50 \times 50$  km. The displacement in ascending and descending unwrapped deformation maps have opposite signs for the same area (Fig. 3b and d); positive displacement is seen in descending deformation maps and negative displacement is seen in ascending deformation maps for the west-wall of the fault. Such a displacement distribution is characteristic of a left-lateral strike-slip motion; this is in agreement with focal mechanism solutions (Table 1). The descending line-of-sight (LOS) displacement is smaller than that in ascending unwrapped interferograms (Figs. 3, 4). Nevertheless, the overall pattern of the coseismic deformation field in ascending and descending observations is consistent (Fig. 3b and d).

Two continuously operated GPS stations, J416 and JB33, are close to the epicentre and are located at the east of the source fault. Detailed GPS data processing is described in Xu et al. (2017); here, we briefly present the data that were utilised in this study. The maximum coseismic displacements were 7.7 cm and 20 cm to the east and north, respectively (Fig. 1c). The observed coseismic offsets are also consistent with left-lateral strike-slip motion on the source fault.

## 3. Slip distribution inversion and fault modelling

S1A differential interferograms in both ascending and descending orbits and GPS data can be used to retrieve seismogenic fault parameters and slip distributions at depth. Focal mechanism solutions given by several organisations indicate that the dip angle of the seismogenic fault varies between  $48^\circ$  and  $84^\circ$ , and the rake angle varies between  $-9^\circ$  and  $-33^\circ$  (Table 1). The relocated aftershocks suggest that the strike of the seismogenic fault is NW (Figs. 1b, 2a). The displacement gradient of the InSAR displacement field indicates the surface traces of

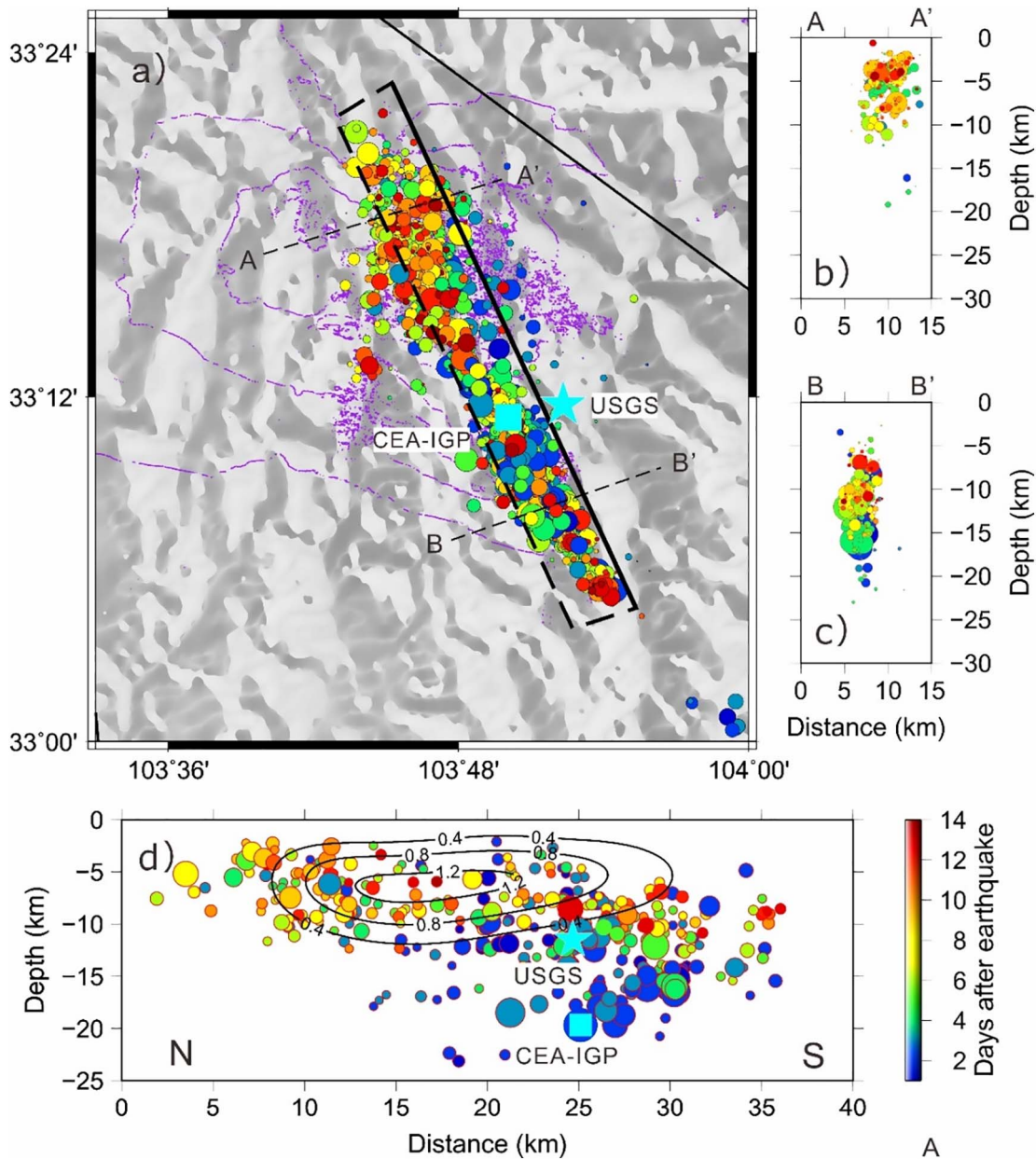


**Fig. 2.** Aftershocks of the Jiuzhaigou earthquake. (a) Spatial distribution of aftershocks of the Jiuzhaigou earthquake. The black rectangle shows the fault model used in the inversion. Purple contours show the distribution of the ascending deformation field acquired from Sentinel-1A SAR data. (b), (c), and (d) show cross sections demonstrating the distributions of relocated aftershocks along the AA' profile, BB' profile, and modelled fault plane in (a), respectively. The contours in (d) show the slip distribution constrained by descending and ascending Sentinel-1A InSAR data and *Global Positioning System* (GPS) data. (For interpretation of the references to colour in this figure legend, the reader is referred to the web version of this article.)

**Table 2**  
Sentinel-1A/IW data parameters used in this study.

No.	Track	Inclination	Master (YYMMDD)	Slave (YYMMDD)	$\Delta T$ (day)	$B_{\perp}$ (m)	Incidence ( $^{\circ}$ )
1	128	Ascending	20170730	20170811	12	35	33.8
2	62	Descending	20170806	20170818	12	48	33.8

the seismogenic fault. By combining these parameters with our InSAR analysis, we conducted a slip distribution inversion using a one-segment fault model. In our model, the lower boundary of the fault is at a depth of 25 km; the length of fault is ~37 km; the strike is 115°, and the rake angles is in the range of (−45°, 45°), implying a left-lateral strike-slip motion. The modelled fault extends from 103.7542°E and

33.3825°N (north-west point) to 103.9224°E and 33.0775°N (south-east point). We used a grid search of the fault dip to determine the dip angle of the source fault; the best-fit result indicates a dip of ~80° to the southwest (Fig. 5). The fault plane was discretised into 750 rectangular patches with a length of 1 km both along strike and downdip. The observed data was modelled in an elastic and homogeneous half-space. In our inversion, only the dip-slip and strike-slip components are estimated for each patch. Based on these parameters, a linear inversion method, Sensitivity Based Iterative Fitting (SBIF), was employed (Wang et al., 2013). The mathematical formulation of the inversion is:

$$f(s) = \sum_{k=0}^K \|D_k - D_k^0 - G_k s(x)\|^2 + \beta^2 \|Hs\|^2 \rightarrow \min \quad (1)$$

where  $s(x)$  is the slip vector,  $k$  is the sign for different input data sets,  $D$  is the matrix of observational data,  $D^0$  is the static offset of observation,

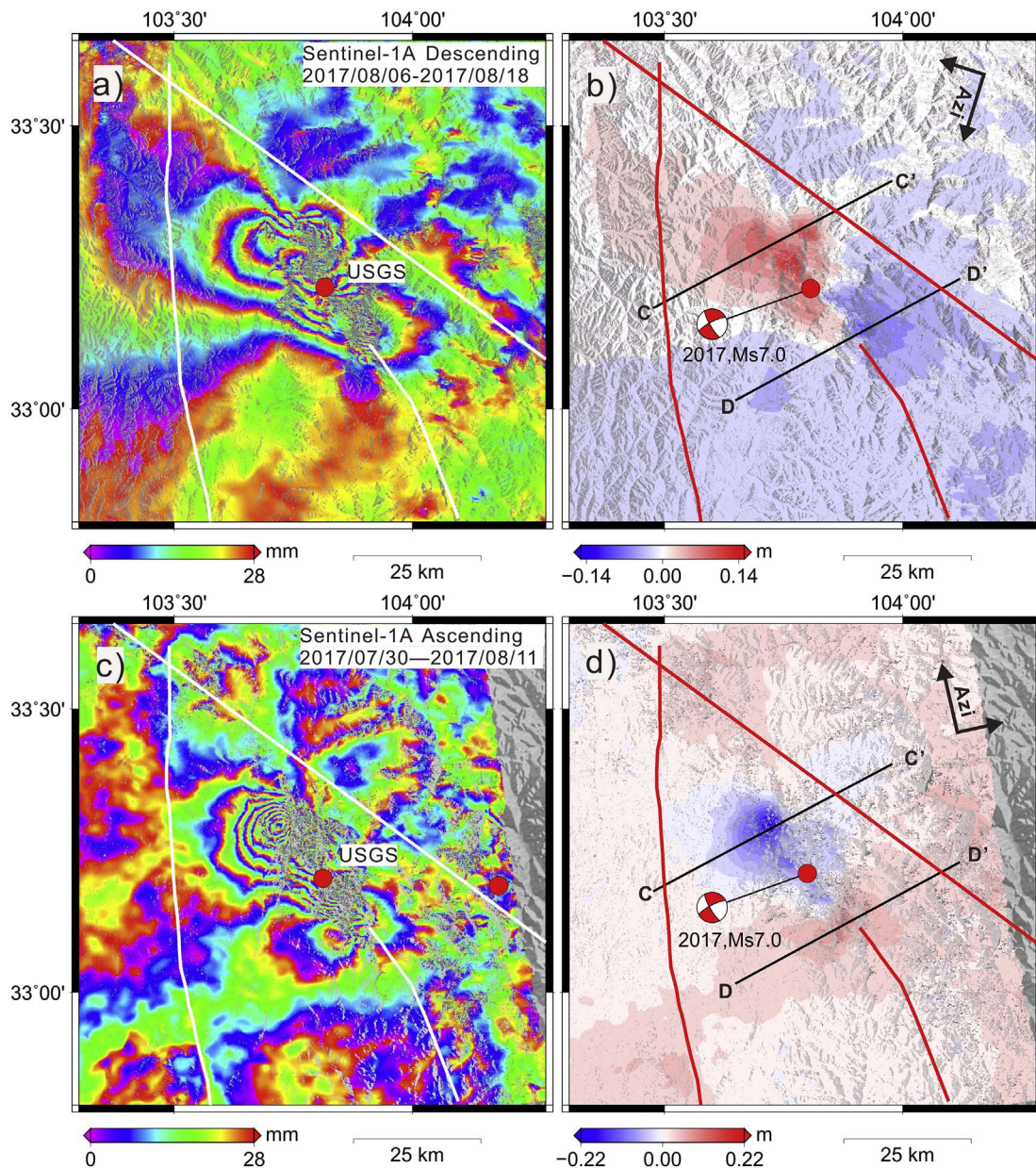


Fig. 3. Coseismic displacement fields of the 2017 Jiuzhaigou Ms7.0 earthquake. Sentinel-1A descending interferograms (a) and displacement field (b). Sentinel-1A ascending interferograms (c) and displacement field (d). The red circles in (a) and (c) represents the epicentre of this event from the United States Geological Survey (USGS). White lines in (a) and (c) and red lines in (b) and (d) denote surrounding active faults. (For interpretation of the references to colour in this figure legend, the reader is referred to the web version of this article.)

$G$  is the Green function for the elastic half-space,  $\beta$  is the smoothing factor,  $H$  is the Laplacian operator, and  $\|Hs\|^2$  is the slip roughness. In this inversion, the Green's function was calculated for the homogeneous elastic half-space model assuming a Poisson ratio of 0.25 using the method described in Okada (1985). For inversion analysis, we resampled the unwrapped interferograms using a uniform decomposition method; each patch was composed of  $35 \times 35$  pixels and the final InSAR dataset consists of  $\sim 7400$  points in descending and ascending measurements.

### 3.1. Slip distribution inversions from S1A ascending and descending data

Using the constructed fault model, we inverted the fault slip distribution under the constraint of decomposed ascending or descending SAR data. Fig. 6a and b show the inverted coseismic slip distributions of the Jiuzhaigou earthquake, as constrained by ascending or descending InSAR measurements. The slip distribution inversion constrained by

ascending InSAR data suggests a concentrated high-slip patch with a magnitude of  $> 0.4$  m at a depth of 5–15 km; a peak slip of 0.9 m occurs at a depth of  $\sim 10$  km. The mean rake angle is  $-24.7^\circ$ , implying a left-lateral strike-slip slip with a slight normal dip-slip component. The inversion constrained by descending data displays a concentrated slip patch at a shallower depth of 0–15 km. The maximum value of this area is  $\sim 1.2$  m at depth of 0–2 km. The mean rake angle is  $-8^\circ$ . Both results suggest that the rupture was dominated by left-lateral strike-slip motion; however, the slip distribution shows different patterns. By comparing these two results with those from preliminary teleseismic waveform analysis (<http://www.cea-igp.ac.cn/>), we can infer that the slip distribution constrained by ascending data is more reasonable. In addition, field investigation also suggests that the rupture did not break the surface. This difference in slip distribution may result from the low quality of data for the near-field of the fault in descending observations. We attempted to invert the slip distribution by masking deformation areas in the descending deformation field and found that the rupture

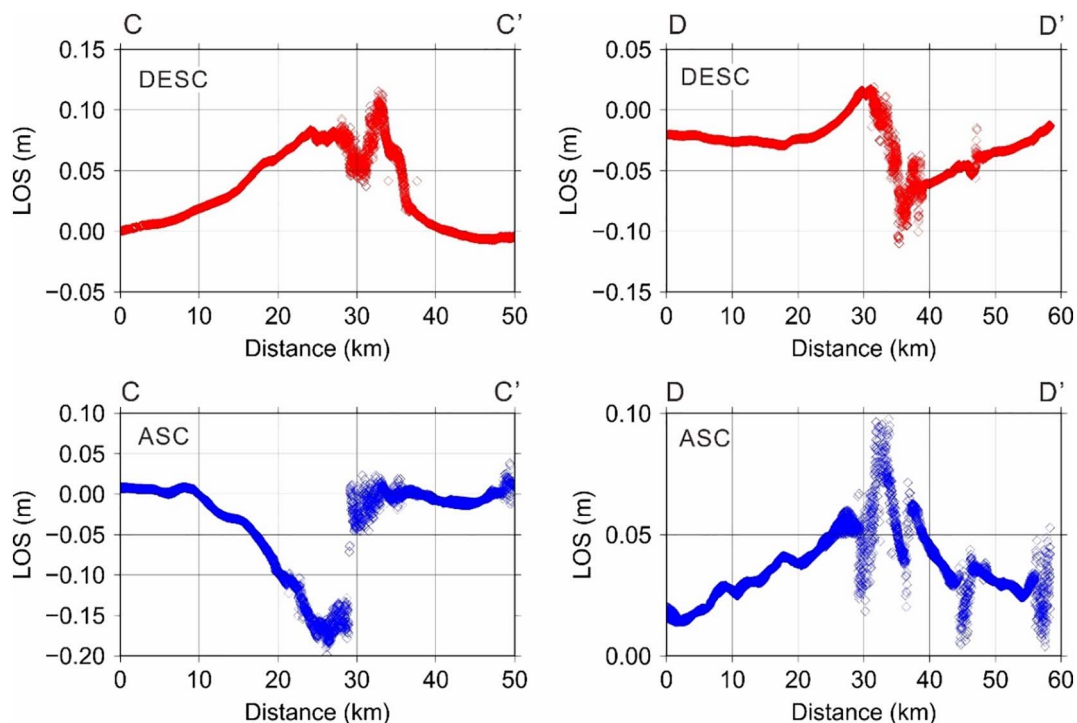


Fig. 4. Line-of-sight (LOS) displacement profiles. (a) LOS in descending InSAR measurements along profile CC'. (b) LOS in descending InSAR measurements along profile DD'. (c) LOS in ascending InSAR measurements along profile CC'. (d) LOS in ascending InSAR measurements along profile DD'. The locations of profiles CC' and DD' are shown in Fig. 3.

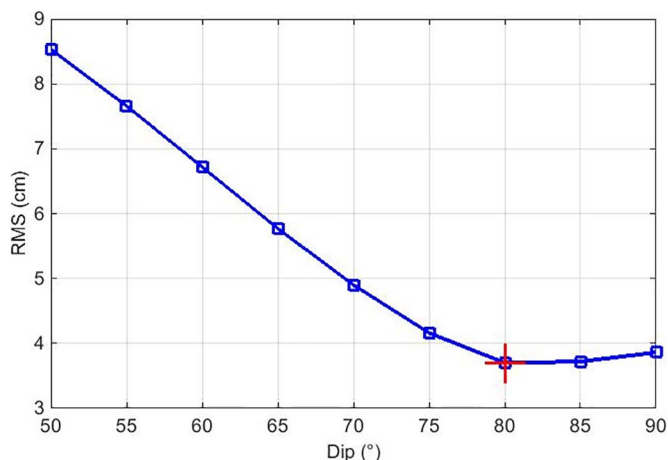


Fig. 5. Trade-off curve between root mean square (RMS) misfit and dip angle for a west-dipping nodal plane. The red cross denotes the optimal dip angle of 80° used to invert the slip distribution. (For interpretation of the references to colour in this figure legend, the reader is referred to the web version of this article.)

still broke the surface. We also inverted the slip distribution under the constraint of ascending InSAR and GPS data (Fig. 5c). The resulting slip pattern was similar to that using just the ascending InSAR data, while the slip magnitude was smaller; peak slip was found to be  $\sim 0.7$  m (Fig. 5a and c).

### 3.2. Joint slip distribution inversion using both InSAR and GPS data

Using the weight ratio 1:1:1, we made a joint fault slip inversion using GPS data, and both ascending and descending InSAR data as constraints (Figs. 6d, 7). We identified a concentrated slip patch located at a depth of 2–15 km; the peak modelled slip was found to be  $\sim 1.3$  m, located at a depth of  $\sim 6$  km. The total seismic moment released by the earthquake rupture was approximately  $6.75 \times 10^{18}$  Nm, corresponding to a moment magnitude of Mw6.5. The slip sense was characterised by

a significant component of left-lateral strike-slip with slight normal dip-slip motion with a mean rake angle of approximately  $-10^\circ$ . Aftershocks were generally distributed on both sides of the rupture area along the fault strike and in an unruptured region along the downdip direction of fault (Figs. 2d, 7). The rupture length of the seismogenic fault was  $\sim 25$  km. The residuals between observed and modelled LOS InSAR measurements and GPS data (Fig. 8) suggest that simulated and observed LOS displacements are well reconciled and that the average residual is  $\sim 6$  cm. However, we observed some significant mismatches between observations and predictions, especially in the near-field of the fault in the joint inversion. The main error source may be low quality data for the near-field of the fault, which is characterised by dense coverage of vegetation. Other possible sources of error include the atmospheric delay, DEM error, inelastic deformation, and simplification of the seismogenic fault.

## 4. Coulomb stress changes analysis

Most aftershocks occurred between 8 August 2017 and 22 August 2017, the largest of which was a M4.8 event, and were characterised by a dominant strike-slip motion (Fang et al., 2017). Previous studies have shown that static Coulomb stress can successfully forecast the approximate location of large damaging aftershocks within months of a large mainshock (Barka, 1999; King et al., 1994; McCloskey et al., 2005; Martínez-Díaz et al., 2012). In order to evaluate static stress changes in the surrounding regions following the Jiuzhaigou earthquake, we calculated Coulomb stress changes using the method of Scholz (1990):

$$\Delta\sigma_c = \Delta\tau_s - \mu(\Delta\sigma_n) \quad (2)$$

where  $\Delta\sigma_c$  is the Coulomb stress change on a specific receiver fault;  $\Delta\tau_s$  and  $\Delta\sigma_n$  are changes in shear and normal stress acting on the receiver fault, respectively; and  $\mu$  is the effective friction coefficient. In following calculation, changes in the shear stress  $\Delta\tau_s$  on a receiver fault are positive;  $\Delta\sigma_n$  is positive for increasing clamping normal stress where pressure is defined as positive. Using the inverted fault slip sources constrained by ascending and descending InSAR and GPS data, we

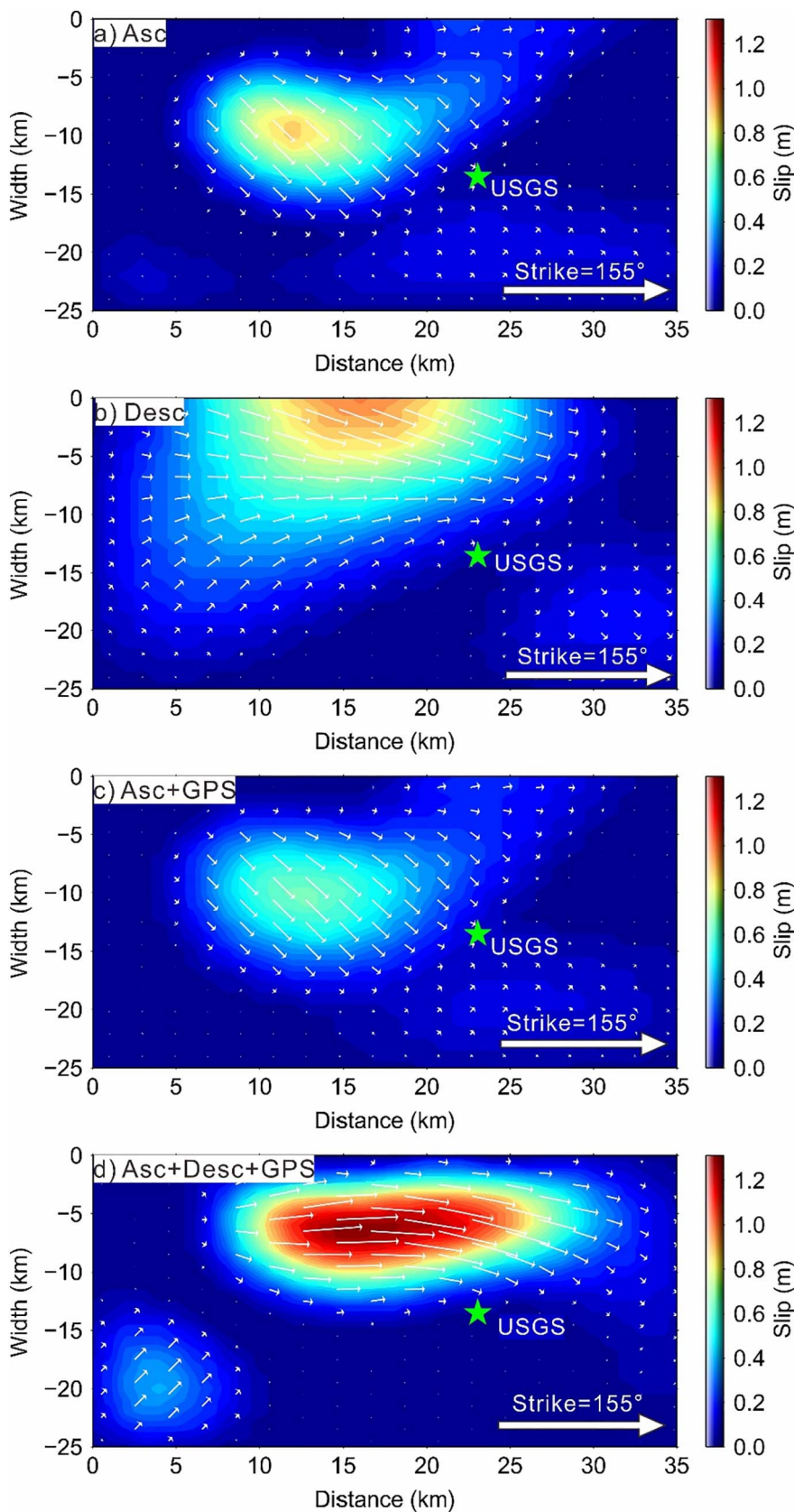


**Fig. 6.** Slip distributions. Slip distributions inferred from inversions constrained by (a) ascending (Asc) InSAR measurements, (b) descending (Desc) InSAR measurements, (c) ascending InSAR measurements and *Global Positioning System* (GPS) data, and (d) ascending and descending InSAR measurements and GPS data. Green stars denote the hypocentre of the Jiuzhaigou earthquake from the United States Geological Survey (USGS). (For interpretation of the references to colour in this figure legend, the reader is referred to the web version of this article.)

adopted a model with variable dislocation sources embedded in an elastic half-space. In this study, a friction coefficient of 0.4 was chosen; this value is suitable for continental strike-slip faults. We resolved the stress at varied depth.

Considering that most of the aftershocks were distributed in a narrow belt along the NNW mainshock rupture zone, we calculated the Coulomb stress changes at different depths, from 5 to 20 km, using a strike-slip plane for receive faults with the same orientation as the



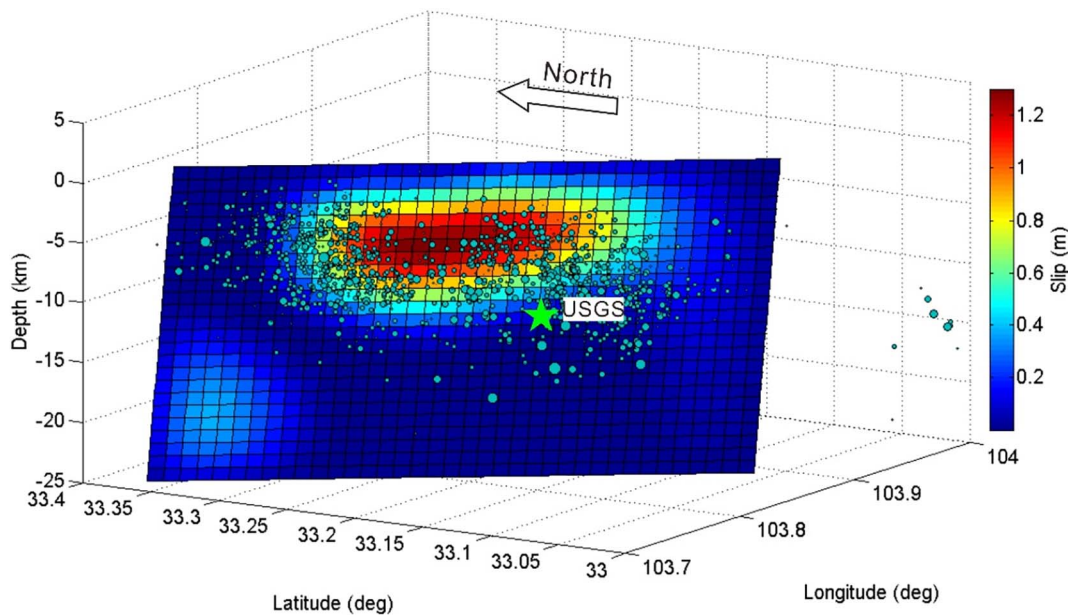


Fig. 7. Perspective view of fault slip and aftershocks distribution of the 2017 Jiuzhaigou Ms7.0 earthquake. The green star denotes the hypocentre of the Jiuzhaigou earthquake from the United States Geological Survey (USGS). (For interpretation of the references to colour in this figure legend, the reader is referred to the web version of this article.)

rupture to reveal the triggering relationship between the mainshock and aftershocks (Fig. 9). Fig. 9a and b show that the largest stress increase appeared on, or near, the mainshock fault plane at a depth of 5 and 10 km, where > 50% of the aftershocks occurred. An obvious stress decreasing zone was observed near the seismogenic fault at a depth of 15 and 20 km, where only a few aftershocks occurred (Figs. 2d, 9c and d); this result indicates that the mainshock mainly triggered aftershocks at depths of 5–10 km. Fig. 2d presents the aftershock distribution along the fault plane; we found that aftershocks occurring within 3 days of the mainshock had a much deeper distribution than those that occurred later. The temporal evolution of the aftershocks towards a shallower depth may have been controlled by stress loading caused by the rupture of the mainshock. It is interesting that the significant stress increasing zone found at a depth of 15 and 20 km in the northern part of the seismogenic fault was without obvious aftershocks (Fig. 9c and d); this may reflect the complex regional crustal structure and fault geometry.

Next, we computed the stress changes on the Minjiang and Tazang faults based on their estimated geometry (Deng et al., 2007; Ren et al., 2013) in order to investigate the influence on these faults on the Jiuzhaigou earthquake (Fig. 10). The results show that the western part of the left-lateral strike-slip Tazang fault was brought 0.1–0.4 MPa closer to failure (Fig. 10a and b), while the southern part of the reverse/left-lateral Minjiang fault saw a Coulomb static stress increase of < 0.1 MPa (Fig. 10c and d). While these regions do not have a historical record of earthquake activity, our results suggest they represent a significant seismic hazard; the Tazang fault in particular requires further study.

## 5. Discussion

### 5.1. Seismogenic fault and tectonic implications

The close proximity of the buried seismogenic fault of this event to the Tazang and the Huya faults raises the question about the relationship and interaction between these faults. The epicentre of 2017 Jiuzhaigou earthquake was located in a triangular zone delimited by the Tazang fault, the Minjiang fault, and the Huya fault (Fig. 1b); however, the relationships and interactions between the seismogenic fault and these active faults remain unknown. Our results indicate that the seismogenic fault of the 2017 Jiuzhaigou earthquake is a buried

strike-slip fault. The northern end is close to the Tazang fault, and the southern end extends up to the Huya fault. We identified it as the northwestward extension of the Huya fault because: (1) the surface trace of the seismogenic fault derived from InSAR and the distribution of relocated aftershocks are both consistent with a northwestward extension of the northern segment of the Huya fault (Figs. 2a, 11); (2) focal mechanism solutions for both the 2017 Jiuzhaigou Ms7.0 event and the 1973 Ms6.5 event indicate a large component of left-lateral strike-slip motion, which is consistent with the northern segment of the Huya fault (Figs. 1b, 11); (3) the Jiuzhaigou earthquake ruptured a seismic gap on the north of the 1976 Songpan earthquake swarm ( $M = 7.2, 6.7, 7.2$ ) and the 1973 Songpan Ms6.5 earthquake (Fig. 11); if this is the case, the 2017 Ms7.0 Jiuzhaigou event, the 1973 Ms6.5 Songpan and 1976 Songpan earthquake sequences ruptured through the Huya fault. This result would imply that the earthquake risk on the Huya fault is decreasing. However, it should be noted that the rupture of the Jiuzhaigou earthquake brought the western segment of the Tazang fault 0.1–0.4 MPa closer to failure, and the southern segment of the Minjiang fault < 0.1 MPa closer to failure (Fig. 10). The Tazang fault has suffered unknown historic ruptures in recent decades (Kirby et al., 2007). The southern part of the northern segment of the Minjiang fault ruptured during a M6.5 event in 1748, a M6.75 event in 1960, and a Ms6.0 event in 1933 (Fig. 11; Table 3). The southern segment of the Minjiang fault ruptured during a Ms7.5 event in 1933 (Fig. 11; Table 3). Thus, the seismic hazard on the Tazang fault is increasing.

### 5.2. InSAR displacement features of the Jiuzhaigou earthquake

The Jiuzhaigou earthquake occurred on a blind left-lateral strike-slip fault without obvious surface rupture. Owing to complex topography and dense coverage of vegetation in this region, it is difficult to investigate the geometry and motion characteristics of this fault through field investigation. However, the InSAR deformation field produced by this event is helpful for our understanding of fault motions and properties. The coseismic displacement fields observed for this event using ascending and descending InSAR data are both distributed asymmetrically on the two sides of the fault with larger measurements on the western wall. Fialko (2006) suggests that the properties of the rock (i.e., the viscosity coefficient variation caused by postseismic relaxation on both sides of the fault) and a parallel faulting structure with

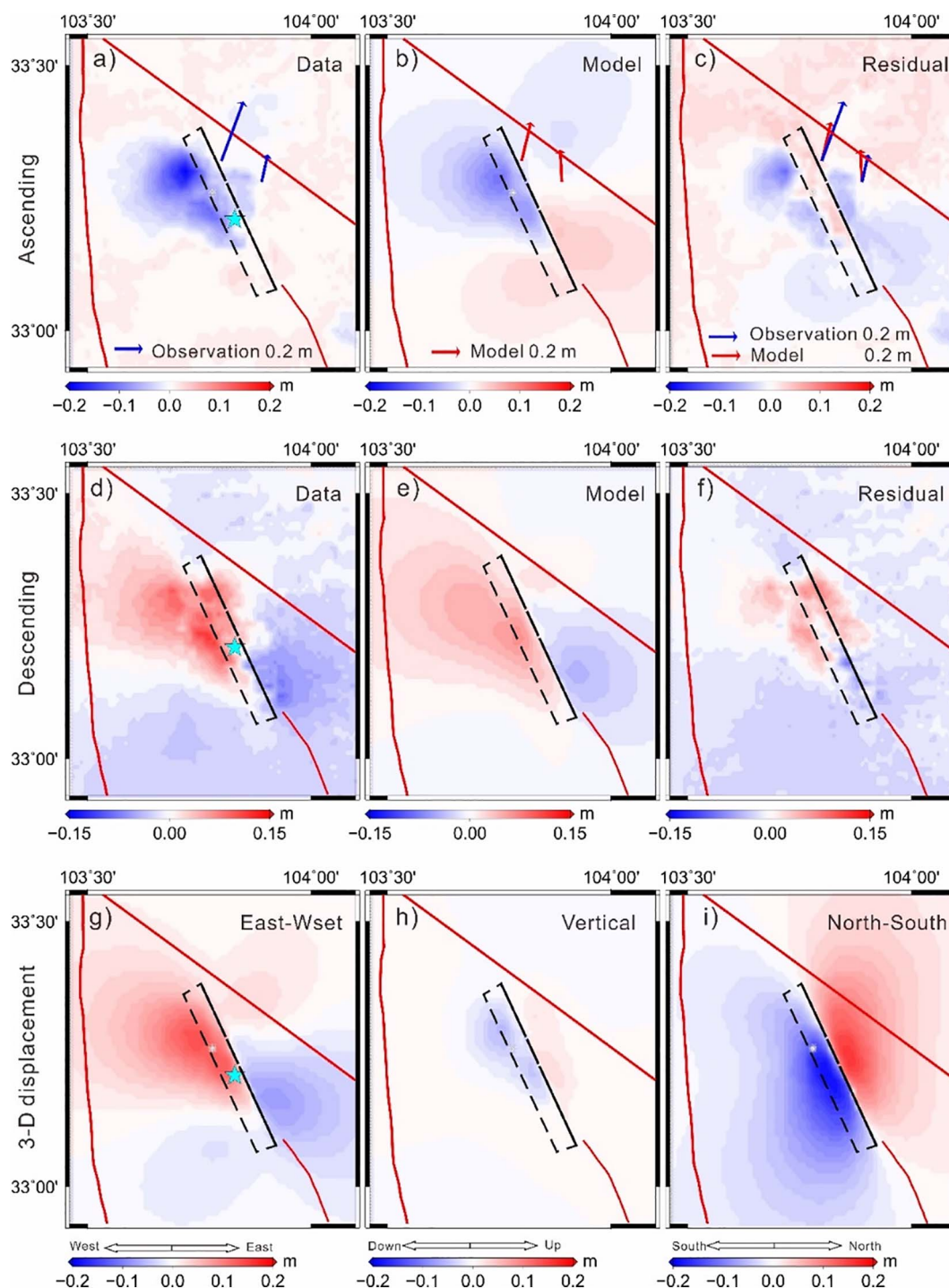


**Fig. 8.** Observed and modelled parameters of the 2017 Jiuzhaigou Ms7.0 earthquake. (a, d) InSAR line-of-sight (LOS) observations, (b, e) model calculations, (c, f) residuals, (g, h, i) modelled 3-D displacement field. Black lines denote the surface projection of the fault plane. Cyan stars denote the earthquake epicentre from the United States Geological Survey (USGS). Red lines denote active faults. (For interpretation of the references to colour in this figure legend, the reader is referred to the web version of this article.)

a low-dip-angle fault would contribute to an asymmetric deformation field caused by rupture of strike-slip faults. Our coseismic interferogram covers only 3 days after the mainshock in the ascending observations and 10 days for the descending observations (Table 2); therefore, postseismic deformation effect can be neglected. The relocated aftershocks indicate an approximately vertical fault plane and our inversion results also indicate a high-dip fault. Therefore, we speculate that the asymmetry of the displacement field produced by this event was mainly caused by complex movement across the fault.

It is common that the LOS displacement field caused by the strike-

slip motion of a fault indicates different patterns. The 2003 Bam (Iran) Mw6.6 earthquake was caused by a predominantly right-lateral strike-slip motion on a subvertical fault; its LOS displacement field was asymmetrical about the fault in both ascending and descending observations and featured a typical quadrantal distribution (e.g., Fialko et al., 2005). The 2010 Yushu (China) Mw6.8 earthquake was a left-lateral strike-slip event that showed different deformation patterns from the Bam earthquake; the typical quadrantal distribution was not obvious in its LOS displacement field (e.g., Qu et al., 2013). The LOS displacement field for the Jiuzhaigou earthquake was largely similar to

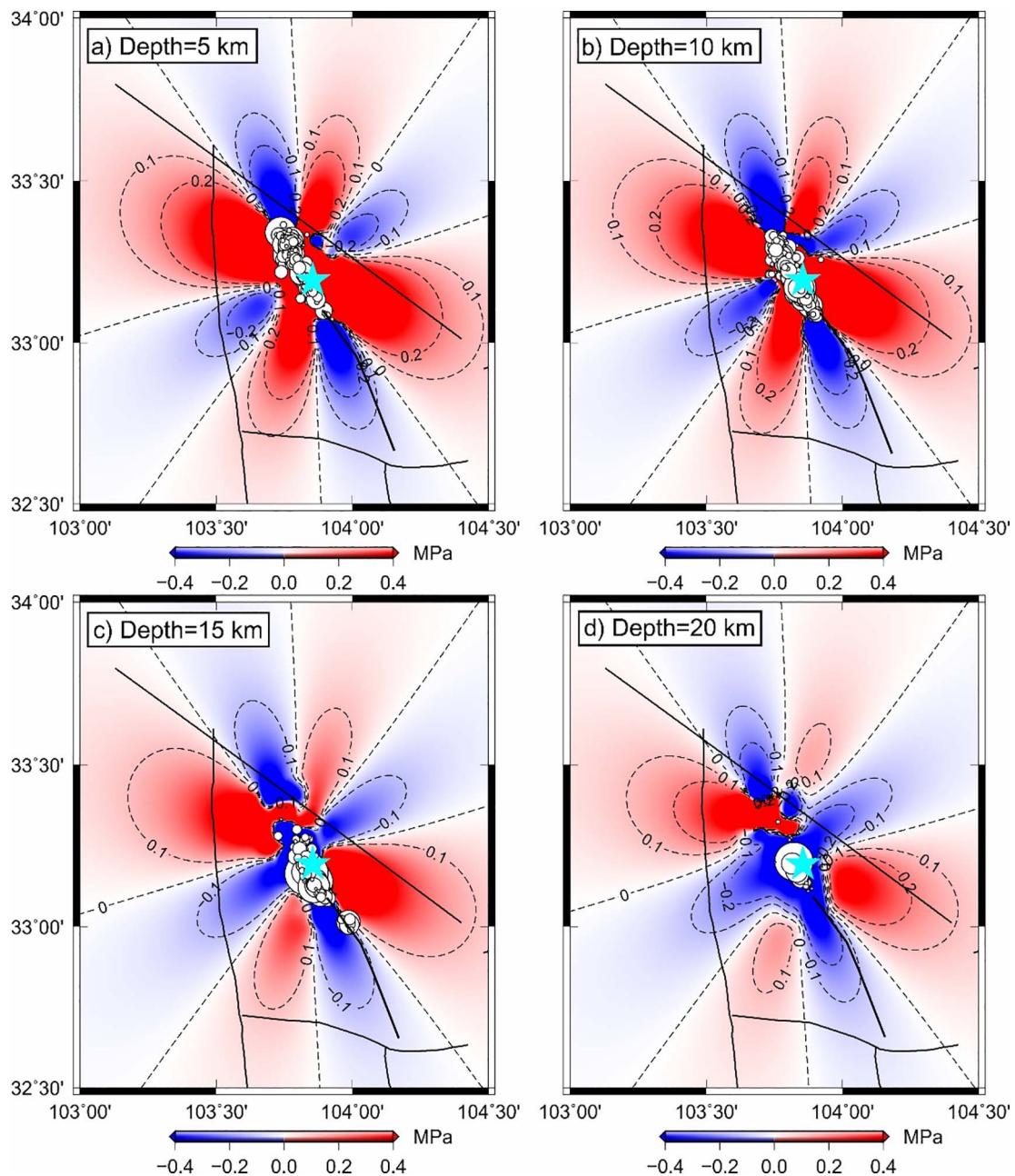
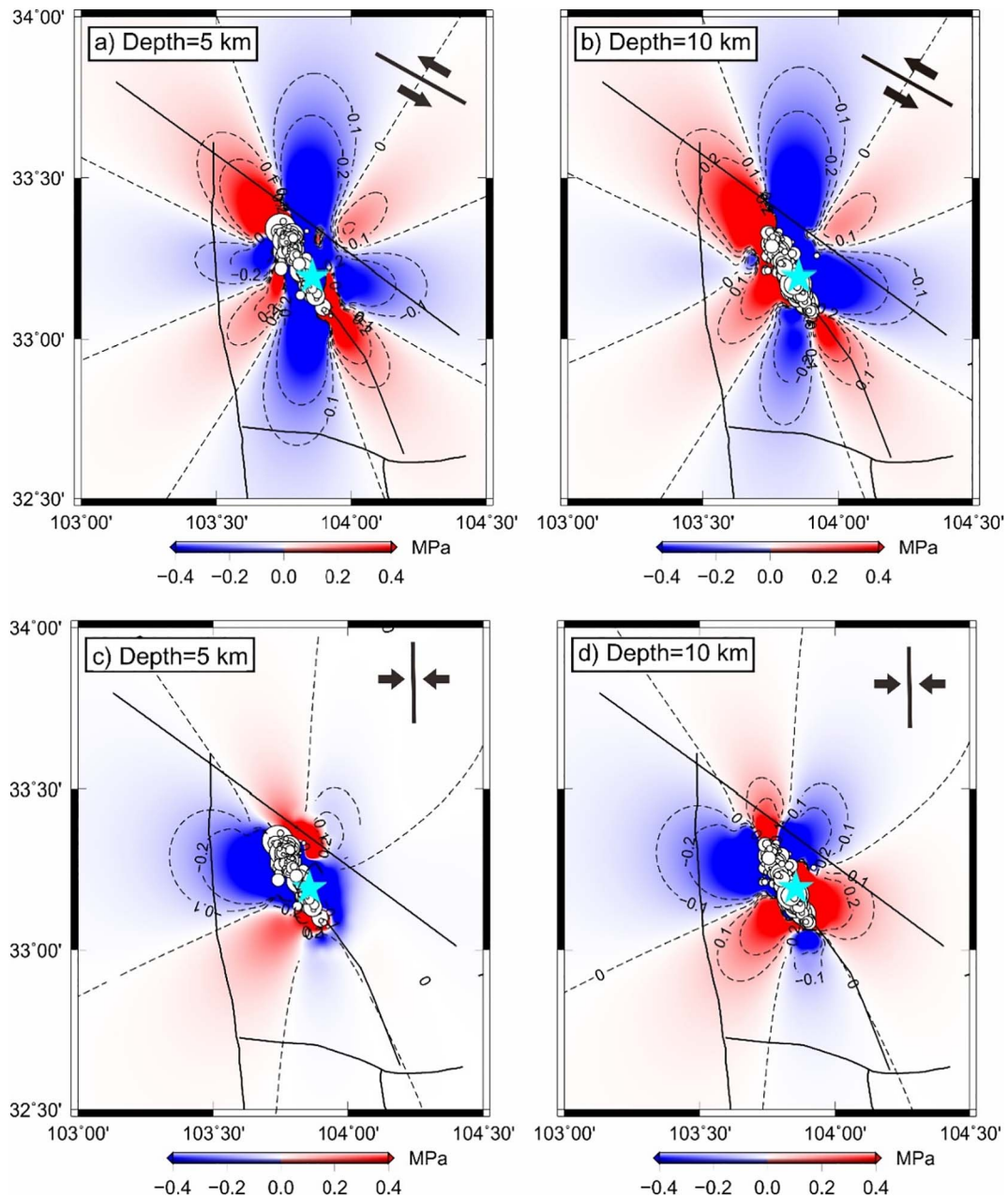


Fig. 9. Static Coulomb stress changes caused by the 2017 Jiuzhaiguo Ms7.0 earthquake on planes with the same orientation as the rupture (i.e., strike = 155°, dip = 80°, rake = -10°). Depth varies from 5 to 20 km. Black lines denote active faults. Cyan stars mark the epicentre from the United States Geological Survey (USGS). White dots represent aftershocks at depths of 0–7 km (a), 7–13 km (b), 13–17 km (c), and 17–22 km (d). (For interpretation of the references to colour in this figure legend, the reader is referred to the web version of this article.)

that of Bam earthquake, having a quadrantal distribution, while the majority of the deformation occurred to the west of the fault in both ascending and descending interferograms (Fig. 2). Indeed, the pattern of the coseismic interferogram is closely related to the geometry and movement of the seismogenic fault.

The total LOS displacements in ascending and descending interferograms largely depend on the contributions of east–west and up–down components; these two components sum constructively or destructively for two sides of a fault. A quadrantal distribution is obvious in east–west and up–down components of the Bam earthquake (Funning et al., 2005); for the Yushu earthquake, the north–south and up–down components feature a quadrantal distribution (e.g., Wang et al., 2014). Little of the north–south motion contributes to InSAR LOS displacement as compared with east–west and vertical components; therefore, in the highly asymmetrical LOS deformation pattern with a quadrantal

distribution, the majority of LOS displacement was on one side of fault in descending or ascending observations of the Bam earthquake (e.g., Funning et al., 2005). East–west displacement was dominant in the Yushu earthquake, so the quadrantal distribution was not obvious. In this study, modelled 3-D displacement components (Fig. 8g, h, and i) show that the quadrantal distribution is obvious only in the east–west component (Fig. 7g). Vertical displacement is characterised by normal dip-slip movement and large displacement occurred on the west wall of the fault (Fig. 8h); north–south displacements contribute little to the LOS measurements (Fig. 8i). The summing of the east–west and up–down components constructively or destructively will mainly affect the deformation pattern in the west wall; the majority of LOS displacement occurred on two sides of the seismogenic fault in descending or ascending observations (Fig. 2b and d); the quadrantal distribution is obvious in the final interferograms (Fig. 2a and c).



**Fig. 10.** Static Coulomb stress changes caused by the 2017 Ms7.0 Jiuzhaigou earthquake. (a, b) Static Coulomb stress changes using NW Tazang as the receiver fault (i.e., strike = 142°, dip = 70°, rake = 0°), as shown in the top right corners of the plots. (c, d) Static Coulomb stress changes using NS Minjiang as the receiver fault (i.e., strike = 88°, dip = 60°, rake = 90°), as shown in the top right corners of the plots.

### 5.3. Relationship with the 2008 Wenchuan Mw7.8 earthquake

The Bayanhar block is a very active sub-block within the Tibetan Plateau. In the last 20 years, seven strong earthquakes (M7–8) have occurred on its boundary faults, including the 2001 Kokoxili Mw7.8, 2008 Wenchuan Mw7.8, and 2013 Lushan Mw6.6 earthquakes (Fig. 1a; Lasserre et al., 2005; Xie et al., 2013; Xu et al., 2009; Xu et al., 2013). The 2008 Wenchuan Mw7.8 earthquake was the strongest recorded event along the eastern boundary of Bayanhar block. The rearrangement of crustal stresses for such a large-magnitude earthquake commonly leads to subsequent damaging earthquakes (Parsons et al., 2000; Stein, 1999). The 2017 Jiuzhaigou Ms7.0 earthquake occurred on a buried fault in the northern part of the eastern boundary of the Bayanhar block. The distance between their epicentres is approximately 250 km, and the distance between the epicentre of the Jiuzhaigou earthquake and the northern segment of the Longmenshan fault belt is

approximately 150 km. A previous study on Coulomb stress changes from the 2008 Wenchuan earthquake interprets that this large-magnitude event brought the Kunlun and Minjiang faults in the eastern Tibetan Plateau 0.02–0.05 MPa closer to failure (Toda et al., 2008). Li et al. (2013) suggested that the Coulomb failure stress change caused by the Wenchuan earthquake showed a significant increase, ~0.05–0.25 MPa, on the Minjiang fault, the Huya fault, and the southeastern segment of the Tazang fault. Huang et al. (2017) showed that coseismic Coulomb stress changes on the hypocentre of the Jiuzhaigou earthquake that were caused by the Wenchuan earthquake were about 8 kPa, and that the postseismic Coulomb stress changes were up to ~12–16 kPa, bringing the Jiuzhaigou earthquake forward by 6–8 years. Wang et al. (2010) compared the accumulation and release of seismic moment in the eastern Tibetan Plateau and suggested that the moment deficit in the Jiuzhaigou epicentral area could produce an Mw6.9 event in the 50 years subsequent to the Wenchuan earthquake.

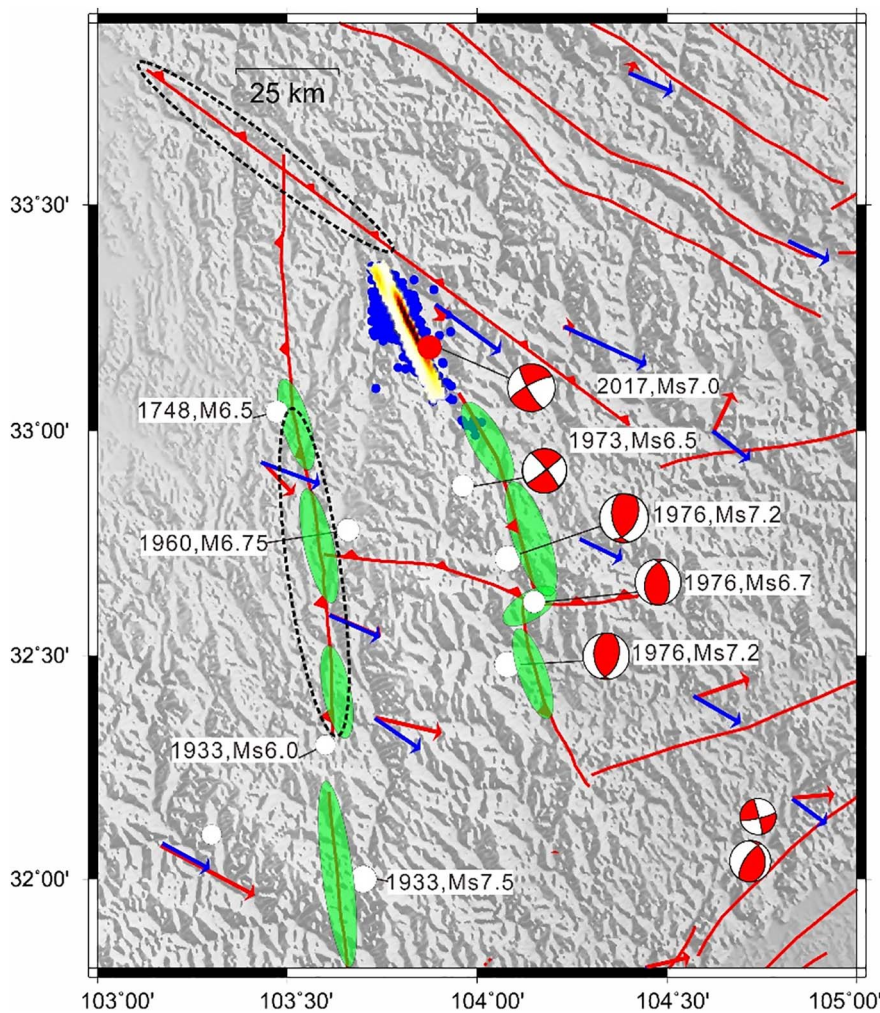


Fig. 11. Approximate rupture areas of historical earthquakes on the Huya and Minjiang faults. Black dashed-line ellipses denote Coulomb stress increasing zones on the Tazang and Minjiang faults. Green ellipses denote approximate rupture lengths; detailed information is listed in Table 3. Blue arrows denote horizontal component Global Positioning System (GPS) velocity vectors relative to stable Eurasia before 2007. Red arrows denote postseismic horizontal component GPS velocity vectors after the 2008 Wenchuan earthquake (data from Li et al., 2017). (For interpretation of the references to colour in this figure legend, the reader is referred to the web version of this article.)

We calculated the coseismic stress changes imparted by the Wenchuan earthquake using the variable slip source models of Zhang et al. (2011) in elastic half-space. We resolved the stress changes at 10 km depth based on the estimated geometry of the Jiuzhaigou earthquake seismogenic fault obtained in this study (Table 3; Fig. 12). The results show a ~5–10 kPa increase in the static stress in the epicentral area of the Jiuzhaigou event along ~35 km of its seismogenic fault. Therefore, it is possible that stress loading from the Wenchuan earthquake had a triggering effect on the Jiuzhaigou earthquake, advancing the date of its occurrence.

### 6. Conclusions

In this study, we mapped the coseismic deformation field of the 2017 Jiuzhaigou earthquake using S1A ascending and descending data.

Obvious displacement from this event was distributed over a  $50 \times 50$  km area. The maximum observed LOS displacements were 0.14 m and 0.22 m in the descending and ascending unwrapped interferograms, respectively. Based on observations from the InSAR data, and on focal mechanism solutions and relocated aftershocks, we constructed a one-segment fault model to invert the slip distribution at depth. Inversions from ascending and descending displacement fields both suggest only one concentrated slip patch, but with different slip patterns. These differences may result from low quality InSAR LOS measurements near the fault. A robust inversion from ascending and descending InSAR data and GPS data shows that the slip mainly occurred at a depth of 2–15 km, with a maximum slip of ~1.3 m. The event was characterised by left-lateral strike-slip motion with a slight normal dip-slip component; the rupture did not break the surface. The results of our joint inversion are consistent with seismological results.

Table 3  
Historic earthquakes and their ruptures on the Minjiang and Huya faults.

No.	Time	Magnitude	Latitude (°)	Longitude (°)	Fault	Rupture length (km)	Study
1	1748	Ms6.5	32.80	103.70	Minjiang	~15	Zhou et al. (2000)
2	1933	Ms7.5	31.9	103.6	Minjiang	> 30	Wang and Shen (2011)
3	1933	Ms6.0	32.30	103.6	Minjiang	~10	Zhou et al. (2000)
4	1960	Ms6.7	32.78	103.67	Minjiang	~15	Deng (2013)
5	1973	Ms6.5	32.93	103.9	Huya	15	Zhu and Wen (2009)
6	1976	Ms7.2	32.72	104.08	Huya	30	Zhu and Wen (2009)
7	1976	Ms6.7	32.62	104.15	Huya	12	Zhu and Wen (2009)
8	1976	Ms7.2	32.48	104.08	Huya	22	Zhu and Wen (2009)

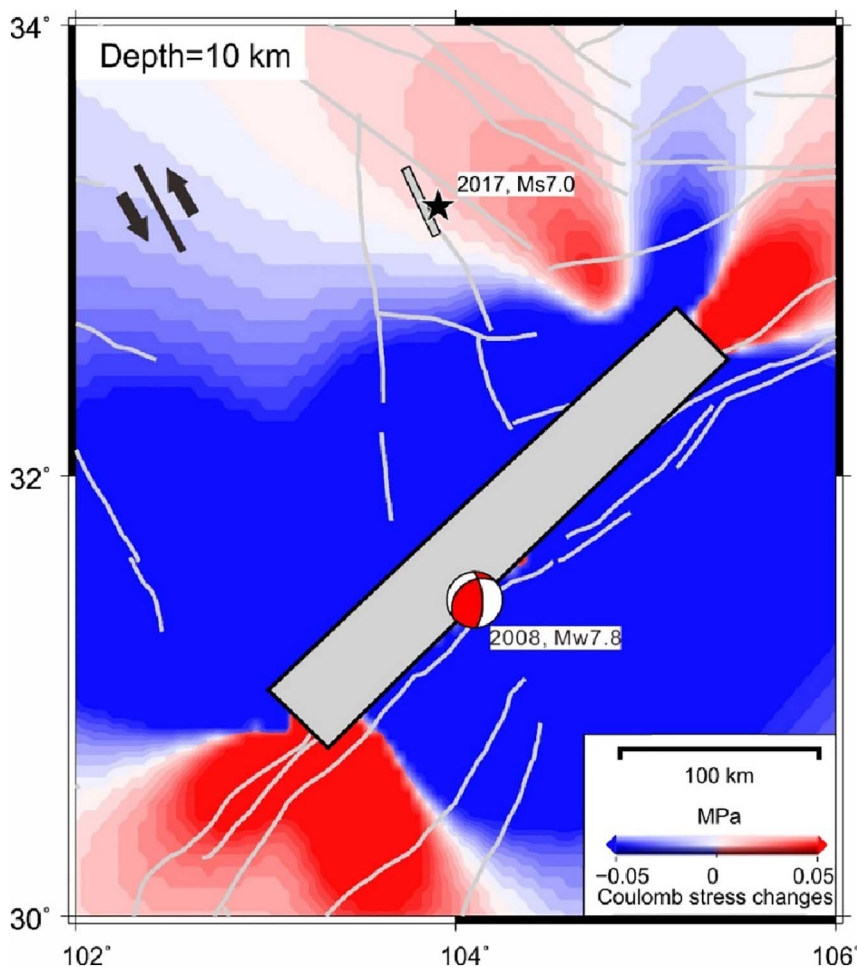


Fig. 12. Coulomb stress changes caused by the 2008 Mw7.8 Wenchuan earthquake at 10 km depth assuming an apparent fault friction of 0.4. The receiver fault is a source fault of the Jiuzhaigou earthquake (i.e., strike = 155°, dip = 80°, rake = -10°). Grey lines denote active faults. Grey rectangles denote surface projections of the fault models for the Wenchuan (south) and Jiuzhaigou earthquakes (north). The black star shows the epicentre of the 2017 Jiuzhaigou earthquake.

The calculation of Coulomb stress changes indicates that the western part of the Tazang fault was brought 0.1–0.4 MPa closer to failure, while the southern part of the Minjiang fault was increased by < 0.1 MPa.

### Acknowledgements

We would like to thank the European Space Agency (ESA) for providing S1A data, and Xu Rui for providing GPS data. This work was supported by the National Key Laboratory of Earthquake Dynamics [grant number LED2015A03] and the National Natural Science Foundation of China [grant numbers 41374015, 41461164002]. Constructive comments and suggestions by three anonymous reviewers led to improvements of the manuscript and are gratefully acknowledged.

### References

- Barka, A., 1999. The 17 August 1999 Izmit earthquake. *Science* 285, 1858–1859.
- De Zan, F., Monti Guarnieri, A., 2006. TOPSAR: terrain observation by progressive scans. *IEEE Trans. Geosci. Remote Sens.* 44, 2352–2360.
- Deng, S.H., 2013. Earthquake on the Longmen MT.-Minshan Fault Zong. *J. Xihua Univ.* 32, 18–22.
- Deng, Q.D., et al., 2007. Active Tectonic Map of China. Earthquake Press, Beijing.
- Deng, Q.D., Gao, X., Chen, G.H., et al., 2010. Recent tectonic activity of Bayanhar fault-block and the Kunlun-Wenchuan earthquake series of the Tibetan Plateau. *Earth Sci. Front.* 17, 163–178.
- Fang, L.H., Wu, J.P., et al., 2017. Relocation of Mainshock and Aftershock Sequences of Ms7.0 Sichuan Jiuzhaigou Earthquake. (unpublished results).
- Fialko, Y., 2006. Interseismic strain accumulation and the earthquake potential on the southern San Andreas fault system. *Nature* 441, 968–971.
- Fialko, Y., Sandwell, D., Simons, M., Rosen, P., 2005. Three-dimensional deformation caused by the Bam, Iran, earthquake and the origin of shallow slip deficit. *Nature* 435, 295–299.
- Funning, G.J., Parsons, B., Wright, T.J., et al., 2005. Surface displacements and source parameters of the 2003 Bam (Iran) earthquake from Envisat advanced synthetic aperture radar imagery. *J. Geophys. Res. Solid Earth* 110, B09406.
- Gan, W., Zhang, P., Shen, Z.K., Niu, Z., Wang, M., Wan, Y., Zhou, D., Cheng, J., 2007. Present-day crustal motion within the Tibetan Plateau inferred from GPS measurements. *J. Geophys. Res. Solid Earth* 112 (B8).
- Goldstein, R.M., Werner, C.L., 1998. Radar interferogram filtering for geophysical applications. *Geophys. Res. Lett.* 25, 4035–4038.
- Grandin, R., Vallée, M., Satriano, C., et al., 2015. Rupture process of the Mw = 7.9 2015 Gorkha earthquake (Nepal): insights into Himalayan megathrust segmentation. *Geophys. Res. Lett.* 42, 8373–8382.
- Harkins, N., Kirby, E.X., Shi, E., Wang, D., Burbank, F., Chun, 2010. Millennial slip rates along the eastern Kunlun fault: implications for the dynamics of intracontinental deformation in Asia. *Lithosphere* 2, 247–266.
- Huang, L.Y., Cheng, H.H., Zhang, H., Shi, Y.L., 2017. Coseismic and Postseismic Stress Evolution Caused by 2008 Wenchuan Earthquake and Its Effects on 2017 Ms 7.0 Jiuzhaigou Earthquake. (unpublished results).
- Jiang, G., Xu, C., Wen, Y., et al., 2013. Inversion for coseismic slip distribution of the 2010 Mw 6.9 Yushu earthquake from InSAR data using angular dislocations. *Geophys. J. Int.* 194, 1011–1022.
- King, C.P., Ross, S., Lin, J., 1994. Static stress changes and the triggering of earthquakes. *Bull. Seismol. Soc. Am.* 84, 935–953.
- Kirby, E., Harkins, N., 2013. Distributed deformation around the eastern tip of the Kunlun fault. *Int. J. Earth Sci.* 102, 1759–1772.
- Kirby, E., Harkins, N., Wang, E., et al., 2007. Slip rate gradients along the eastern Kunlun fault. *Tectonics* 26, TC2010.
- Lasserre, C., Peltzer, G., Crampé, F., et al., 2005. Coseismic deformation of the 2001 Mw = 7.8 Kokoxili earthquake in Tibet, measured by synthetic aperture radar interferometry. *J. Geophys. Res. Solid Earth* 110, B12408.
- Li, P., Zhang, J.Z., Li, X.G., 1979. A survey on the 1933 Diexi earthquake and some new knowledges of its seismogenetic structure. In: *A Compilation of Seismo-geological Survey in Sichuan-Yunnan Intensive Earthquake Regions*. Seismological Press, pp. 62–76.
- Li, Y.J., Chen, L.W., Lu, Y.Z., Zhan, Z.M., 2013. Numerical simulation on influences of Wenchuan earthquake on the stability of faults in the neighborhood. *Earth Sci. J. China Univ. Geosci.* 38, 398–410.
- Li, Y.C., Zhang, G.H., Shan, X.J., et al., 2017. Fault Coupling of the Longmenshan Fault

- Before and After the 2008 Wenchuan Mw 7.9 Earthquake Constrained by GPS Data and Its Tectonic Implications. (unpublished results).
- Martínez-Díaz, J.J., Bejar-Pizarro, M., Álvarez-Gómez, J.A., et al., 2012. Tectonic and seismic implications of an intersegment rupture: the damaging May 11th 2011 Mw 5.2 Lorca, Spain, earthquake. *Tectonophysics* 546–547, 28–37.
- McCloskey, J., Nalbant, S.S., Steacy, S., 2005. Indonesian earthquake: earthquake risk from co-seismic stress. *Nature* 434, 291.
- Okada, Y., 1985. Surface deformation due to shear and tensile fault in a half-space. *Bull. Seismol. Soc. Am.* 82, 1018–1040.
- Parsons, T., Toda, S., Stein, R.S., et al., 2000. Heightened odds of large earthquakes near Istanbul: an interaction-based probability calculation. *Science* 288, 661–665.
- Prats-Iraola, P., Scheiber, R., Marotti, L., Wollstadt, S., Reigber, A., 2012. TOPS interferometry with TerraSAR-X. *IEEE Trans. Geosci. Remote Sens.* 50, 3179–3188.
- Qu, C.Y., Zhang, G.H., Shan, X.J., Zhang, G.F., Song, X.G., Liu, Y.H., 2013. Coseismic deformation derived from analyses of C and L band SAR data and fault slip inversion of the Yushu Ms7.1 earthquake, China in 2010. *Tectonophysics* 584, 119–128.
- Ren, J., Xu, X., Yeats, R.S., et al., 2013. Millennial slip rates of the Tazang fault, the eastern termination of Kunlun fault: implications for strain partitioning in eastern Tibet. *Tectonophysics* 608, 1180–1200.
- Scholz, C.H., 1990. *The Mechanics of Earthquakes and Faulting*. Cambridge Univ. Press, New York (439 pp.).
- Solaro, G., De Novellis, V., Castaldo, R., et al., 2016. Coseismic fault model of Mw 8.3 2015 Illapel earthquake (CHILE) retrieved from multi-orbit sentinel1-A dInSAR measurements. *Remote Sens.* 8, 323.
- Stein, R.S., 1999. The role of stress transfer in earthquake occurrence. *Nature* 402, 605–609.
- Tang, R.C., Lu, L.K., 1981. On the seismogeological characteristics of 1976 Songpan-Pingwu earthquakes (in Chinese with English abstract). *Seismol. Geol.* 3, 41–47.
- Tang, R.C., Jiang, N.Q., Liu, S.L., 1983a. Recognition of the geological setting and the seismogenic condition for the Diexi magnitude 7.5 earthquake. *J. Seismol. Res.* 6, 327–338 (in Chinese with English abstract).
- Tang, R.C., Liu, S.L., Jiang, N.Q., Wang, Y.H., Wang, X.M., 1983b. The 1933 Diexi Earthquake. Sichuan Scientific and Technological Press (69 pp.).
- Toda, S., Lin, J., Meghraoui, M., et al., 2008. 12 May 2008 M = 7.9 Wenchuan, China, earthquake calculated to increase failure stress and seismicity rate on three major fault systems. *Geophys. Res. Lett.* 35, L17305.
- Wang, K., Shen, Z.K., 2011. Location and focal mechanism of the 1933 Diexi earthquake and its associated regional tectonics. *Acta Seismol. Sin.* 33, 557–567.
- Wang, H., Liu, M., Shen, X., et al., 2010. Balance of seismic moment in the Songpan-Ganze region, eastern Tibet: implications for the 2008 Great Wenchuan earthquake. *Tectonophysics* 491, 154–164.
- Wang, R., Parolai, S., Ge, M., et al., 2013. The 2011 Mw 9.0 Tohoku earthquake: comparison of GPS and strong-motion data. *Bull. Seismol. Soc. Am.* 103, 1336–1347.
- Wang, X.W., Liu, G.X., Yu, B., Dai, K., Zhang, R., Chen, Q., Li, Z.L., 2014. 3D coseismic deformations and source parameters of the 2010 Yushu earthquake (China) inferred from DInSAR and multiple-aperture InSAR measurements. *Remote Sens. Environ.* 152, 174–189.
- Wen, Y., Xu, C., Liu, Y., et al., 2013. Coseismic slip in the 2010 Yushu earthquake (China), constrained by wide-swath and strip-map InSAR. *Nat. Hazards Earth Syst. Sci.* 13, 35–44.
- Werner, C., Wegmüller, U., Strozzi, T., et al., 2000. Gamma SAR and interferometric processing software. In: *Proceedings of the ERS-Envisat Symposium*, Gothenburg, Sweden, pp. 1620.
- Xie, Z.J., Jin, B.K., Zheng, Y., et al., 2013. Source parameters inversion of the 2013 Lushan earthquake by combining teleseismic waveforms and local seismograms. *Sci. China Earth Sci.* 56, 1177–1186.
- Xu, X., Wen, X., Yu, G., et al., 2009. Coseismic reverse-and oblique-slip surface faulting generated by the 2008 Mw 7.9 Wenchuan earthquake, China. *Geology* 37, 515–518.
- Xu, X.W., Wen, X.Z., Han, Z.J., et al., 2013. Lushan Ms 7.0 earthquake: a blind reserve-fault event. *Chin. Sci. Bull.* 58, 3437–3443.
- Xu, R., Liao, H., Liu, Y.F., et al., 2017. Interpretation of Seismic Characteristics of 2017 Jiuzhaigou M7.0 Earthquake Based on Near-field GPS Data. (unpublished results).
- Zhang, G.H., Qu, C.Y., Shan, X.J., et al., 2011. Slip distribution of the 2008 Wenchuan Ms 7.9 earthquake by joint inversion from GPS and InSAR measurements: a resolution test study. *Geophys. J. Int.* 186, 207–220.
- Zhou, R.J., Pu, X.H., He, Y.L., et al., 2000. Recent activity of Minjiang fault zone, uplift of Minshan block and their relationship with seismicity of Sichuan. *Seismol. Geol.* 22, 285–294 (in Chinese with English abstract).
- Zhu, H., Wen, X.Z., 2009. Stress triggering process of the 1973 to 1976 Songpan, Sichuan, sequence of strong earthquake. *Chin. J. Geophys.* 52, 994–1003 (in Chinese with English abstract).